Energy loss and electron and x-ray emission of slow highly charged Ar^{q+} ions in grazing incidence on an Al(111) surface

Xianwen Luo, Bitao Hu,* Chengjun Zhang, Jijin Wang, and Chunhua Chen
School of Nuclear Science and Technology, Lanzhou University, 730000 Lanzhou, People's Republic of China
(Received 3 December 2009; published 17 May 2010)

Within the framework of the classical over-barrier model, energy loss, electron emission, and x-ray emission of slow highly charged ion Ar^{q+} grazing on the Al(111) single-crystal surface under various azimuthal angles have been studied. The enhancement of energy loss, potential electron emission yields, intensity of KL^1 satellite lines, or x-ray yields for the Ar^{17+} ion grazing along low-index crystallographic directions was observed. The calculated energy-loss spectra of atomic projectiles Ar^0 interacting with metallic surface agree reasonably well with experiment. The inner-shell filling contributions through the side feeding mechanism, Auger transitions, and the radiative decay process are discussed by analyzing the final charge-state distributions of the reflected ions, potential electron emission yields, and x-ray yields under different azimuthal angles.

DOI: 10.1103/PhysRevA.81.052902 PACS number(s): 34.50.Bw, 79.20.Hx, 78.70.En, 61.85.+p

I. INTRODUCTION

Many experimental and theoretical studies of ion or atom-surface scattering under grazing angles have been performed in the past few years [1–5]. In the majority of cases, ion or atom-surface interactions are accompanied by inelastic processes [6], such as the electronic energy loss, which can favorably be studied using channeling [3]. Information on ion or atom-surface interactions was mainly obtained by measuring emitted electrons [1] and x ray [7]. Some measurements of the final charge-state distributions of reflected ions were done [8,9]. In addition, the energy loss which depends on the neutralization of projectiles above the surface can provide additional information on the ion-surface interaction [10]. Most of these studies have been performed for atomic or multicharged projectiles, but not for highly charged ions [1–5,8].

When the slow highly charged ions (SHCI) (with $v < v_0$, where v_0 is Bohr velocity) approach crystal surface, the electrons from the solid surface can be captured to high-lying empty shells of SHCI in a very short time and leave the low shells empty. As a result, the exotic atomic species (i.e., the "hollow atoms") are formed [11–14]. This initial stage of SHCI-surface interaction seems to be well described by a classical over-barrier model (COBM) [15,16], which is applicable above the surface. These "hollow atoms" spontaneously decay to their ground states via a cascade of Auger transitions or x ray. However, the de-excitation rates are insufficiently fast to explain the high neutralization and relaxation of reflected ions [9,17]. Therefore, the side-feeding (SF) mechanism, which is now known as the direct transfer of electrons from target states into inner shells of ion, was proposed by Winecki *et al.* [18,19]. Although the over-barrier model has been successful in describing side-feeding neutralization above the surface, the contributions of the side-feeding mechanism to the filling of inner-shell vacancies is still a matter of discussion.

Electron emission as a consequence of SHCI interacting with metal surfaces shows a number of interesting features [20–22], and was traditionally ascribed to two different mechanisms of kinetic electron emission (KEE) and potential electron emission (PEE). The kinetic electron emission of He° atom and He^+ ion scattering from an Al(111) surface under grazing incidence was investigated by Winter *et al.*, and the target current recorded as a function of azimuthal angles was enhanced for scattering along low-index crystallographic directions [23]. In the work of Hughes *et al.*, the total electron yields of N^{2+}, N^{5+}, and N^{6+} ions incident on the Au(011) single-crystal surface were studied with the velocity ranging 0.25–0.55 a.u. [24]. The researchers observed that total electron yields strongly depend on the crystal azimuthal angle. So far, to the best of our knowledge, no investigation of the correlation between PEE yields and the crystal azimuthal angle can be found.

X-ray spectra have been previously employed by d'Etat *et al.* [25] to investigate the decay of *K*-shell vacancies for the interaction of Ar^{17+} ions on metallic surface at grazing incidence. Their experiment has determined the intensity of $K\alpha$ lines for different incidence angles, from 6.5° to 3°. The researchers observed that the intensity of KL^x satellite lines depends on the incidence angle. In particular, the intensity of the KL^8 line strongly decreases at small incidence angles. However, the dependence of the intensity of $K\alpha$ lines and the corresponding x-ray yields on azimuthal angles is still unknown. A lot of research has been devoted to the energy loss of SHCI grazing from surfaces [24,26,27]. In the work of Hughes *et al.*, the inelastic energy loss as a function of crystal azimuthal orientation was presented [24]. Because the incident angle of ionic N^{q+} projectiles was chosen as 20°, many of these projectiles can traverse a target of finite thickness. Consequently, the corresponding energy loss can be interpreted as a sum of two components; one occurred above the surface and the second happened after traversing the finite thickness target. Therefore, we assume that the result is still not clear for the dependence of the energy loss on the crystal azimuthal angle for SHCI at grazing incidence.

The neutralization of SHCI also can be studied by detecting final charge-state distributions of reflected ions [17,18]. In the work of Winecki *et al.* [18], the $Ar^{q+}(q = 2–17)$ ions, with velocities ranging from 0.15 to 0.62 a.u., were used. For final charge-state Ar°, the fraction decreases as the velocity increases because the hollow atom spends less time above the

*hubt@lzu.edu.cn

surface as the incident velocity increases. When HCI grazes on the crystal surface, the hollow atom spends more time under "axial channeling," which takes place if the direction of the incident projectile is close to a major crystal axis (low-index directions). For the same reason, the fraction of final charge-state Ar^0 should change for HCI grazing along low-index directions in comparison to random directions. However, we still lack evidence to confirm the dependence of final charge-state distributions on azimuthal angles because no one has previously paid attention to this issue.

In this paper, we try to find the dependence of total energy loss, PEE yields, and intensity of $K\alpha$ lines on crystal azimuthal angles. The organization of the paper is as follows. In the following sections, the theoretical aspects for the motion of ion, energy loss, and mechanism of electron emission are presented, and then the calculation results will be discussed and compared with the corresponding experimental results. A short conclusion will be presented in Sec. IV.

II. THEORETICAL ASPECTS

A. Ion's motion

For grazing ion-surface scattering, trajectories are predominantly determined by the interatomic interaction potential between projectiles and lattice atoms. In addition, trajectories might also be affected by dielectric response phenomena, which create an "image charge." Therefore, an SHCI with charge state q_1 at a distance R from the metallic surface is subjected from two forces:

$$\vec{F}(q,R) = F_{\rm im}\hat{e}_x + \sum \vec{F}_{\rm TFM}(R), \tag{1}$$

where the first item is image force, which always accelerates the ionic projectiles toward metallic surface, and can be given by

$$F_{\rm im}(R) = \frac{q_1(R)^2}{4R}, \tag{2}$$

and the second one is the sum of the forces experienced by SHCI from all target atoms. The force that the SHCI experienced by one target atom can be given by

$$\vec{F}_{\rm TFM}(R) = \frac{d}{dR}[W_{\rm TFM}(R)], \tag{3}$$

where the $W_{\rm TFM}(R)$ is the Coulomb potential between projectile and a target atom. The interaction potential for atomic species with atomic numbers Z_1 and Z_2 separated by a distance r can be approximated by screened Coulomb potentials of this type:

$$W_{\rm TFM} = \frac{Z_1 Z_2}{r}\phi(r/a_F), \tag{4}$$

where $\phi(r/a_F)$ is an interatomic "screening function." In our simulation, we adopted the Thomas-Fermi-Moliere screening function as follows:

$$\phi(r/a_F) = \sum_i a_i \exp(-b_i r/a_F), \tag{5}$$

in which $a_i = \{0.35, 0.55, 0.1\}$, $b_i = \{0.3, 1.2, 6.0\}$. a_F is the screening length:

$$a_F = \frac{0.8854}{\sqrt{(Z_1 - q_1)^{2/3} + (Z_2 - q_2)^{2/3}}}, \tag{6}$$

where q_1 and q_2 are the charge states of projectiles and target atom, respectively. In order to simplify the calculation, when ion or atom-surface distances $R > 5.0$ a.u., the interaction potential between ion and target atoms can be approximated by a continuum potential [6]:

$$\sum W_{\rm TFM}(R) = 2\pi n_s Z_1 Z_2 a_F \sum_i \frac{a_i}{b_i}\exp(-b_i R/a_F), \tag{7}$$

where n_s is the number of surface atoms per unit area. Equation (7) shows that the continuum potential depends only on the distance R normal the surface plane.

By using these forces, the ion's motion was simulated by a stepwise integration of the Newton equations of motion, using 1 a.u. time steps. This process, including trajectories length calculation, charge exchange, etc. was carried out using a Monte Carlo program written by our group and the simulations were initiated with the HCI positioned outside the range of the first charge transfer. In the vicinity of the surface, the HCI is attracted by the image charge and will eventually undergo close collisions with the surface. When the HCI approaches the first atomic plane, the repulsive forces will become stronger than the attractive one and the HCI will be specularly reflected. We only consider the situation when the projectiles are reflected specularly from the first atomic layer, which means that the incidence angle should be taken to be the order of some degrees. The present simulation used a single-crystal aluminum target with clean and flat surface. As shown in Fig. 1, the surface channels are along the directions of $[1,0,\bar{1}]$ and $[0,1,\bar{1}]$, etc. A coordinate system is placed in the scattering plane with the y, z axis parallel to the surface and the x axis perpendicular to the surface. According to the Debye model, thermal vibrations are included by calculating random displacements of the target atoms with a surface Debye temperature, and the Debye temperature of 390 K is taken for two dimensions of surface plane.

B. Charge-exchange processes

According to the COBM [15], the critical distance R_c where the first charge transfer takes place, can be given by

$$R_c \approx \frac{1}{2W}\sqrt{8q+2}, \tag{8}$$

where q is the initial charged state of projectiles and W the work function of metallic surface. Within the critical distance R_c, charge transfer between HCI and solid surface occurs mainly through resonant processes and Auger transitions. The Cowan code was adopted to calculate the intra-atomic Auger rate for $n > 3$ in vacuum:

$$\mathrm{A}_{n,n'} = \frac{5.06\times 10^{-3}}{|\Delta n|^{3.46}}, \tag{9}$$

where $\Delta n = n\text{-}n'$ is the smallest allowed quantum jump between the initial n and n' final quantum number of bound electrons. For inner-shell (K-,L-, and M-shell) Auger

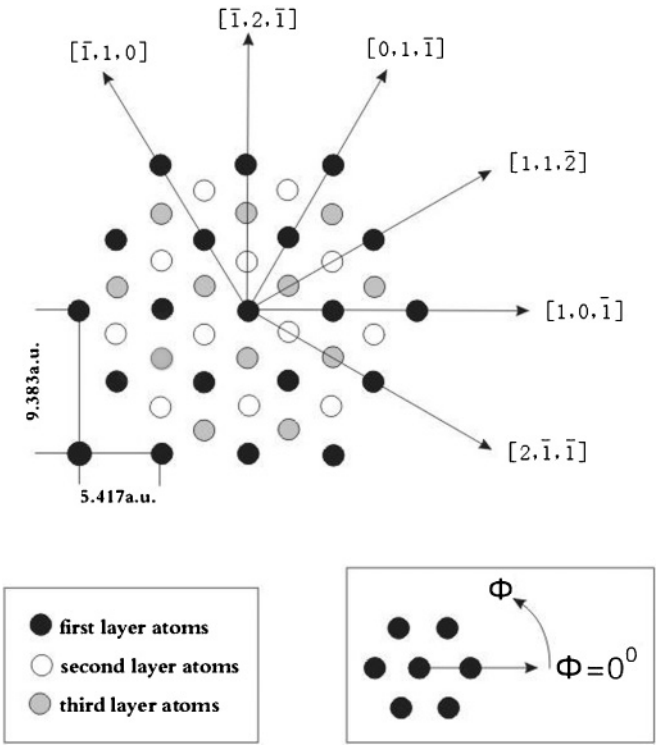

FIG. 1. Sketch of the Al(111) surface structure.

transitions rates given by Ref. [18] were used. A theoretical analysis of the neutralization dynamics above the surface has been presented on the basis of the classical over-barrier model (COBM) [15], including the resonant multielectron capture of conduction electrons, the resonant loss into unoccupied states of conduction band, and the intra-atomic Auger de-excitation. The population P_n of the $n_{\rm th}$ shell can be described by a rate equation:

$$\begin{aligned}\frac{dP_n}{dt} &= \theta(S_n - P_n) I_n^{\rm RC} - I_n^{\rm RL} P_n \\ &+ \theta(S_n - P_n) w_n^{\rm fin} \sum_{n'>n} A_{n',n} w_{n'}^{\rm ini} - 2 w_n^{\rm ini} \sum_{n'<n} A_{n,n'} w_{n'}^{\rm fin} \\ &- I_n^{\rm PO} P_n + \theta(S_n - P_n) I_n^{\rm SF} \\ &+ \theta(S_n - P_n) \sum_{n'>n} \Gamma_{n',n} - \sum_{n'<n} \Gamma_{n,n'}, \end{aligned} \tag{10}$$

where $I_n^{\rm RC}$ and $I_n^{\rm RL}$ are the current of resonant captured and lost electrons, $I_n^{\rm PO}$ is the decay rate of peeling off process, $I_n^{\rm SF}$ is the electron capture rate of the side-feeding (SF) process, $w_n^{\rm ini}$ and $w_n^{\rm fin}$ are the (empirical) statistical factors to correct the Auger rate $A_{n',n}$, $\Gamma_{n,n'}$ is the radiative decay rate, S_n is the number of electrons fully filled of the $n_{\rm th}$ shell, and θ is the unit step function.

C. Energy loss

The energy loss that SHCI experiences along its trajectory can be interpreted as a sum of two components: (i) elastic energy loss and (ii) inelastic energy loss.

1. Elastic energy loss

The elastic energy loss can be easily calculated from the binary collisions between projectiles and lattice atoms as follows [10],

$$\Delta E_{\rm el} = E_0 \left[1 - \left(\frac{\cos\theta \pm \sqrt{(\mu^2 - \sin^2\theta)}}{1+\mu} \right)^2 \right], \tag{11}$$

where E_0 denotes the initial kinetic energy of projectiles, θ the scattering angle, and $\mu = m_t/m_p$ (m_t and m_p are the mass of projectiles and lattice atoms). The plus sign will be applied for $m_p \leqslant m_t$; otherwise, the minus sign is chosen.

2. Inelastic energy loss

The inelastic energy loss comes from three sources, namely: (i) charge-exchange energy loss, (ii) large-distance energy loss, and (iii) electron energy loss.

(i) Accompanying the charge exchange of SHCI with the metallic surface, a part of kinetic energy is taken away by exchanged electrons. The charge-exchange energy loss can be described as a soft collision, in which momentum conservation only in the direction of incident beam needs to be imposed [28]. In our simulation, P, T, and m stand for projectiles, target atoms, and electrons, respectively. If the surface electrons are captured to the high-lying level of SHCI, that is, $P + (T + m) \rightarrow (P + m) + T$ process, the charge-exchange energy loss can be given by

$$\Delta E = B_T - B_P + E_P \frac{m_p}{4m_T} \left(\frac{m_p + m}{m_p} \frac{B_T - B_P}{E_P} - \frac{m}{m_p} \right)^2, \tag{12}$$

where m_P, m_T, and m denote the mass of projectiles, lattice atoms, and electrons; B_p and B_T the binding energy of exchanged electrons; and E_p the energy of projectiles. When the electron resonant loss is into the unoccupied states of the crystal surface, that is, the $(P + m) + T \rightarrow P + m + T$ process, B_T contributes a minor part to the energy loss and can be neglected. Hence, the charge-exchange energy loss can be given by

$$\Delta E = \frac{1}{2} m v^2 + \frac{m_p}{m_p + m} B + E_P \frac{m_p}{4m_T} \left(\frac{B}{E_P} \right)^2, \tag{13}$$

where v denotes the laboratory-frame velocity of the projectiles, $B = B_P + E_C, E_C$, the mean kinetic energy of electron separated from the projectiles [29].

(ii) When the highly charged ions are placed in front of the metallic surface, electrons in the surface and the bulk will be polarized and build up an induced charge density. If the ionic projectile is moving with finite parallel velocity, the induced charge density will lag behind the ion, leading to an additional force in the direction opposite to that of the ion velocity. This force represents the so-called friction force or stopping power, which comes from two contributions of particle-hole and plasmon excitations. The surface loss function which is the key quantity for the calculation of the stopping power can be given by [30]

$$g(Q,\omega) = \frac{Q}{2\pi} e^{2QR} \langle R | \Phi_{\rm ind}(Q,\omega) | R \rangle, \tag{14}$$

where $\Phi_{\rm ind}(Q,\omega)$ is the induced potential. The imaginary part of $g(Q,\omega)$ provides the key input to the stopping power calculation as follows:

$$\mathrm{Im}\{g_{\rm SRM}(Q,\omega)\} = \mathrm{Im}\{g^{\rm pl}_{\rm SRM}(Q,\omega)\} + \mathrm{Im}\{g^{\rm ph}_{\rm SRM}(Q,\omega)\}, \tag{15}$$

where $S^{\rm ph}_{\rm SRM} = \mathrm{Im}\{g^{\rm ph}_{\rm SRM}(Q,\omega)\}$ and $S^{\rm pl}_{\rm SRM} = \mathrm{Im}\{g^{\rm pl}_{\rm SRM}(Q,\omega)\}$ represents the stopping power due to the particle-hole excitation and the collective plasmon excitation, respectively. According to Ref. [30], these stopping powers can be given by

$$\begin{aligned} S^{\rm pl}_{\rm SRM} &= \frac{\gamma_0 v}{8\omega_s^2}\frac{1}{\left(R + c^{\rm pl}_{\rm SRM}\right)^3} \\ S^{\rm ph}_{\rm SRM} &= \frac{3v\ln(0.983 q_{\rm TF}R)}{2\pi q^4_{\rm TF}}\frac{1}{R^4}, \end{aligned} \tag{16}$$

where v stands for the parallel velocity of ionic projectile, γ damping factor ($\gamma = 0.03$ a.u. for the aluminum target), r_s Wigner-Seitz radius, $\omega_s = \omega_p/\sqrt{2}$, $\omega_p = \sqrt{(3/r_s^3)}$ the classical surface plasmon frequency, $q_{\rm TF} = (12/\pi)^{1/3}/\sqrt{r_s}$ Thomas-Fermi wave number, and $c^{\rm pl}_{\rm SRM} = 3.56$. By using the above expressions, the stopping power for unit charged ($q = 1$) projectile can be obtained. Therefore, when an HCI grazes on the metallic surface, the calculation for large-distance energy loss can be performed by using the stopping power, which can be given by

$$S(q_1,R,v) = q_1^2\left(S^{\rm ph}_{\rm SRM} + S^{\rm ph}_{\rm SRM}\right), \tag{17}$$

where q_1 is the charge state of a projectile.

(iii) In the present simulation, when the projectile is close enough to reach electron gas of the metallic surface ($R \leqq 5.0$ a.u.), the electron energy loss process begins and its values can be obtained by integrating the position-dependent stopping power [27]:

$$S_e(R) = 2k_F^2\frac{v}{v_F}\int_0^1 kdk[\sigma_n(k)]^2 H(k,z_0'), \tag{18}$$

where R is the distance from the top surface layer, $z_0' = R - r_d$, $r_d = 2.99$ a.u. is the average atomic radius of the aluminum target, and $k_F = v_F$ is the Fermi wave number, according to the Brandt-Kitagawa (B-K) model [31], in terms of the expression (18):

$$\sigma_n(k) = Z_1\frac{q(R) + (2kk_F\wedge)^2}{1 + (2kk_F\wedge)^2}, \tag{19}$$

where Z_1 is the atomic number of projectiles, Λ a screening length, and $q(R)$ the position-dependent ionization degree. Because low-velocity ions are highly neutralized before they reach the closest distance from the surface [9], an exponentially decaying function was adopted to model the electron transition rate [32]. When $R > r_d$, the position-dependent ionization degree can be expressed as

$$q(R) = q_0\exp\left[-\exp\left(-\frac{R - z_s}{L}\right)\right], \tag{20}$$

where q_0 is the initial ionization degree and L is a characteristic length, $z_s = L\ln(\Gamma_0 L/v_n)$ with v_n being the perpendicular velocity and Γ_0 a typical resonant ionization rate. But, for $R < r_d$, an empirical model based on the velocity-dependent electron-stripping criterion in which the ionization degree shows a good agreement with experimental values for heavy ions was adopted:

$$\begin{aligned} q_b = 1 - \exp\big(&0.803y_r^{0.3} - 1.3167y_r^{0.6} \\ &-0.38157y_r - 0.008983y_r^2\big), \end{aligned} \tag{21}$$

where $y_r = v_r/Z_1^{2/3}$, with v_r being the ion velocity relative to the target-electron velocity, defined in Ref. [27]. In (18), the detailed expressions for $H(k,z_0')$ are provided in Refs. [27,33]. The electron energy loss dE experienced by the projective ion moving dL distance can be calculated as follows:

$$dE = S_e(R)dL, \tag{22}$$

where $S_e(R)$ characterizes position-dependent stopping power, and dL is effective ion and atom-surface interaction length (i.e., the part of the trajectory in which ions interact efficiently with surface electron gas). For analyzing the effective trajectory length, it is necessary to define a starting point for the effective trajectory. Because the electron energy loss process is switched on only when the projectile is close enough to the metallic surface, the effective trajectory length is computed only when $R \leqq 5.0$ a.u.

D. Electron emission

1. *Kinetic electron emission*

Because the excited electron induced during binary collisions between projectiles and surface conduct electrons [34] needs to overcome the vacuum-metal potential barrier (appropriate surface work function W) to escape from the metal surface, a classical velocity threshold of incident projectiles must be taken into account. In 1979, Baragiola *et al.* [35] gave the KE velocity threshold as follows:

$$v_{\rm th} = \frac{v_F}{2}\left[\left(1 + \frac{W}{E_F}\right)^{1/2} - 1\right]. \tag{23}$$

For $v_p < v_{\rm th}$, the maximum momentum transferred to electrons is insufficient for the excited electron to overcome its binding energy. When the final kinetic energy of the excited electron is larger than the surface potential (10.6 eV for the aluminum target), the ejection of the electron into vacuum happens.

2. *Potential electron emission*

The formation and decay of hollow atoms can make a significant contribution to the observable "above surface" potential electron emission yields, namely: (i) autoionization of the excited hollow atoms, due to its decay by cascade Auger or radioactive decay, (ii) promotion loss of electrons previously captured by HCI due to their combined action of self- and image-charge screening near the surface, (iii) peeling off of all electrons still bound in highly excited projectile states at the moment of HCI reaching the metal surface [36].

One important process which is missing in Eq. (10) but actually switched on in our physical model is the promotion

loss process. The classical model for promotion loss can be explained by the electron energy level, which is given by [15]

$$\varepsilon_n = -\frac{q_n^2}{2n^2} + \frac{q - 1/2}{2R}, \tag{24}$$

where q_n is the effective charge state of HCI felt by an electron on the $n_{\rm th}$ shell, which can be calculated by the Slater rule [37], q is the charge state of the HCI at distance R. the first term is the binding energy of the atomic energy level of the $n_{\rm th}$ level, and the second one is the modification caused by the image charge of HCI. When the HCI approaches the metal surface, the projectile energy level ε_n will be shifted upward due to the screening of the already captured electron and the repulsive interaction of self-image [i.e., the action of the first and the second terms in Eq. (24)]. With the decrease of q_n and R, ε_n will be larger than zero at a certain distance and electrons on the $n_{\rm th}$ shell can escape into a vacuum, which is called the promotion loss process.

For the peeling off, when the HCI approaches the surface, the outer shells are continually populated with weak binding energy and large orbital radius (comparable to the critical electron resonant capture distance R_c). It is assumed that when $r < r_n + z_j - \lambda_{\rm scr}$, the outer orbital electrons are likely to move to valence-band continuum if their classical radii r_n exceed the screening length $\lambda_{\rm scr}$, where r is the distance between the HCI and the image plane of the surface and z_j is the average distance from jellium to the topmost surface layer [38]. These electrons may be peeled off by the target atoms or stop in the target. If they are not peeled off, they will return to the original orbit of HCI. In the present study, we used the peeling off cross section, which is the product of the screened Rutherford scattering cross section $\sigma_{\rm sn}$ for free electrons colliding with target atoms [39,40] and the modification factor $F(E_0)$, modifying $\sigma_{\rm sn}$ for the bounded electron. The emission rate of peeling off the electron is expressed as

$$I_n = \nu_n L N \sigma_{\rm sn} F(E_0), \tag{25}$$

where ν_n is the electron orbital frequency, L is the overlapped orbital length of the HCI and target, N is the density of the target atom, E_0 is the energy level of outer shell electrons, and n is the main quantum number. The detailed expressions for the screened Rutherford scattering cross section $\sigma_{\rm sn}$ are provided in Ref. [41] and references therein.

E. X-ray emission

X-ray spectrum is very important for us to study the inner-shell charge exchange for its clock property [25], involving the matching of the energy of x-ray lines and the electron distribution of the atom while de-exciting. When slow highly charged ions Ar^{17+} graze on the surface, the K x-ray spectra consist of two peaks due to $K\alpha$ and $K\beta$ transitions. According to Ref. [18], the transition rates (both Auger and radiative decay) are expressed as a function of the shell populations, and the $K\alpha$ and $K\beta$ decay rates can be obtained by $\Gamma = 3.04 \times 10^{-4}(2 - n_K)n_L\Theta(n_L - 1)$ and $\Gamma = 2.49 \times 10^{-5}(2 - n_K)n_M\Theta(n_M - 1)$, where n_K, n_L, and n_M are the electron numbers of the K, L, and M shells and $\Theta(n_n - 1)$ is the step function. The $K\alpha$ decay may take place at any time of the L-shell filling, and one observes the $K\alpha$ transition in the presence of any number x ($x = 1$–8) of L spectator electrons. Because the de-excitation rate of $K\beta$ decay is much smaller than that of $K\alpha$, the $K\beta$ transition is neglected here to simplify the calculation. In order to simulate the K-shell x-ray spectra, energies of KL^x lines are expected as a function L- and M-shell populations. The following approximate expression for $K\alpha$ energies was adopted [18,42],

$$E_{K\alpha} = 3144.3 - 22.2n_L - 4.9n_M + 0.4n_Ln_M\,(\text{eV}). \tag{26}$$

III. RESULTS AND DISCUSSION

A. Energy loss

For an incident ion, the energy-loss calculation starts as soon as the charge-exchange processes begin, which means that the energy-loss processes can already begin at a relatively large distance from the surface. The critical distance for the beginning of the energy-loss processes depends on the initial charge state of the ions and work function of the surface. For example, the critical distance is equal to 37.5 a.u. for the Ar^{17+} ions incident on the aluminum target ($W = 4.26$ eV). For atomic projectiles, the energy-loss processes begin only when the projectiles are close enough to the metallic surface so that the electron energy loss process can switch on. Thus, only the electron energy loss contributes to the inelastic energy loss. The calculated energy loss is given by the difference between the kinetic energy of reflected particles and the primary energy of projectiles.

Figure 2 shows energy-loss spectra obtained from 12-keV argon atoms grazing on the Al(111) surface under incidence of $\theta_{\rm in} = 2.2^\circ$. The interaction of atomic projectiles Ar° grazing on the metallic surface was performed for random directions, which is consistent with the initial conditions in Ref. [43]. The calculated average total energy loss is 92.9 eV, and the

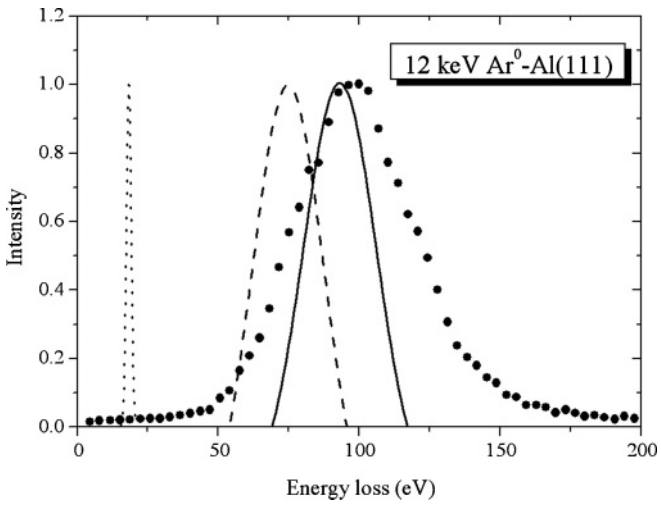

FIG. 2. Energy loss spectra for 12-keV argon atoms grazing on the Al(111) single-crystal surface under incidence of $\theta_{\rm in} = 2.2^\circ$. (Solid circles) Experimental results of Ref. [43]. (Curves) Results from the present calculation (dotted curve, elastic energy loss; dashed curves, inelastic energy loss; solid curve, summation of elastic and inelastic energy loss, i.e., total energy loss).

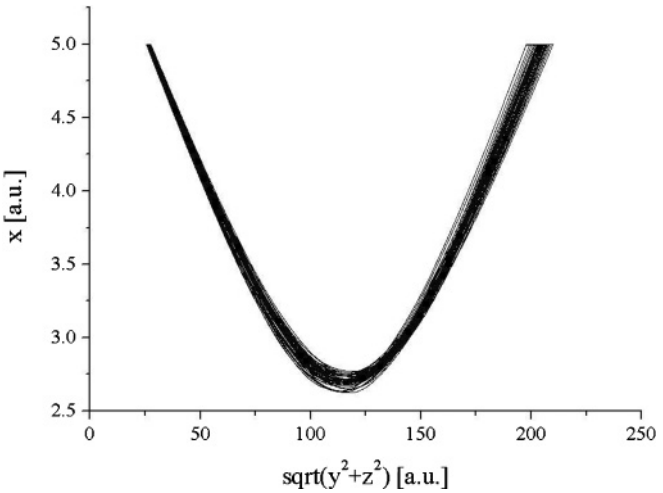

FIG. 3. Trajectories for 12-keV Ar° atoms grazing on the Al(111) surface under random directions; x stands for the distances from the projectiles to the topmost surface layer and sqrt(y^2+z^2) are the distances parallel to the single-crystal surface plane.

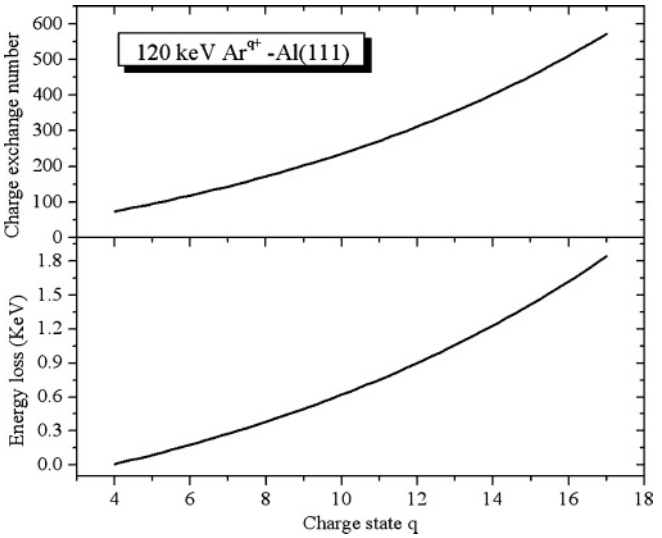

FIG. 4. The charge-exchange number and charge-exchange energy loss as a function of the initial charge state of 120-keV Ar^{q+} ($q = 4$–17) grazing on the Al(111) surface at $\theta_{in} = 0.8°$.

energy-loss spectra agree reasonably with the experimental data. However, the calculated energy-loss spectra do not look the same as the already published spectra [44], in which the small intensity peak at the high-energy side developed in the main peak of $\Phi = 10°$ spectra (i.e., the tail of the spectra was found). This feature has been explained by the two different classes of trajectories, which are assigned to different contributions in the energy-loss spectra. Therefore, a careful trajectory analysis is needed for the analysis of energy-loss spectra. In our case, the calculated trajectories for 12-keV argon atoms grazing on the Al(111) surface under random directions was shown in Fig. 3 and the existence of different classes of trajectory was not found. Therefore, the contributions to energy-loss spectra result from the same class of trajectories. Consequently, there are no tails in the calculated energy-loss spectra.

In Fig. 4, we plot the charge-exchange number and charge-exchange energy loss as a function of the initial charge state of projectile argon grazing on the Al(111) surface at an incident angle $\theta_{in} = 0.8°$. In the present work, five charge-exchange mechanisms of resonant capture, resonant loss, Auger transition, and peeling off and side-feeding processes are taken into account since they happen throughout the HCI-surface interaction process. As shown in Fig. 4, the charge-exchange number increases with the increasing of the initial charge state of projectiles, and charge-exchange energy loss also increases with the increasing of initial charge states because more electrons are exchanged at higher charge state. For example, several hundreds of electrons are exchanged for slow highly charged ions Ar^{17+} grazing on the metallic surface, and the corresponding charge-exchange energy loss contributes a lot to the total energy loss for highly charged ions grazing on the Al(111) surface.

Figure 5 shows the total energy losses of highly charged ions Ar^{17+} with incident energy 120-keV grazing at different azimuthal angles. If the azimuthal angle of the plane of incidence coincides with a low-index direction on the crystal surface plane, grazing can occur along strings of surface atoms in the regime of "axial channeling." Therefore, when the Ar^{17+} ions graze along a low-index direction (e.g., $[1,0,\bar{1}]$ or $[0,1,\bar{1}]$) of surface plane, "axial channeling" happens. Otherwise, "planar channeling" happens if the Ar^{17+} ions grazing is along random directions. According to the present simulation, the effective trajectory length $dL \approx 413$ and 345.5 a.u. for 120-keV Ar^{17+} ions grazing along low-index and random directions, respectively. From Eq. (22), electron energy loss will increase if the projectiles experience longer effective trajectory length. Thus, the dependence of total energy loss on azimuthal angles is enhanced when Ar^{17+} ions are grazing along the low-index directions. These results strengthen the conclusion that the dependence of total energy loss on azimuthal angles is from the effect that the effective trajectory length can be prolonged by the axial channeling

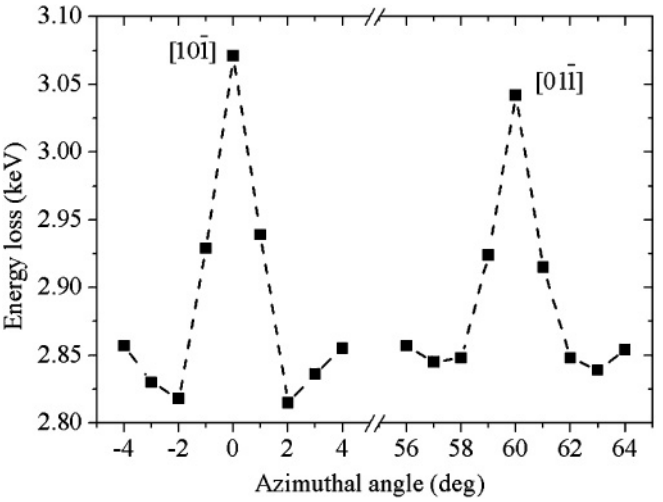

FIG. 5. The total energy loss of 120-keV Ar^{17+} grazing on the Al(111) surface under incidence of $\theta_{in} = 0.8°$. Incident azimuthal angles are around $\varphi = 0°$ and $\varphi = 60°$. The dashed lines are drawn to guide the eyes.

along the very axis (e.g., [1,0,$\bar{1}$], [0,1,$\bar{1}$]). Grazing projectile scattering provides a new technique for nondestructive surface structure determination ("surface triangulation"), because the enhanced electron yield can already be observed by an increase of the target current when incident beams are changes from planar to axial surface scattering [45]. By using this method, the low-index crystallographic directions are found from this current change as a function of the azimuthal orientation of the target surface. In addition, from Fig. 5, we have reason to believe that information about the structure of the crystal surface also can be obtained by studying the energy loss of HCI as a function of the azimuthal orientation of the target surface.

B. Electron emission

1. Kinetic electron emission

According to Ref. [45], a classical modeling of near-KE-threshold behavior was adopted to calculate KE yields.

Figure 6 shows kinetic electron yields of experimental and calculated results with incident velocity ranging from 0.055 to 0.148 a.u. The KE yields increase with the increasing of incident velocity. Because when the incident velocity increases, more kinetic energies of projectiles are transferred to conduction electrons in binary encounters. When incident velocities of argon atoms $v \geqslant 0.125$ a.u. ($E > 11.85$ keV), calculated results agree well with experimental data. The KE yields are less than 0.49 per ion when incident energies of argon atoms are lower than 21.85 keV.

2. Potential electron emission

In Ref. [41], the N shell and higher orbits, particularly the continuum orbits, are treated together as one shell labeled C, so only the inner shell (K, L, M) for SF processes are important. Under the $Z_{\rm ion} < Z_{\rm solid}$ condition ($Z_{\rm ion}$ and $Z_{\rm solid}$ denote the atomic number of incident ions and target atoms, respectively), the average contribution to the filling of different shells through SF mechanism increases with the increasing of the quantum number of shells. In particular, the contribution

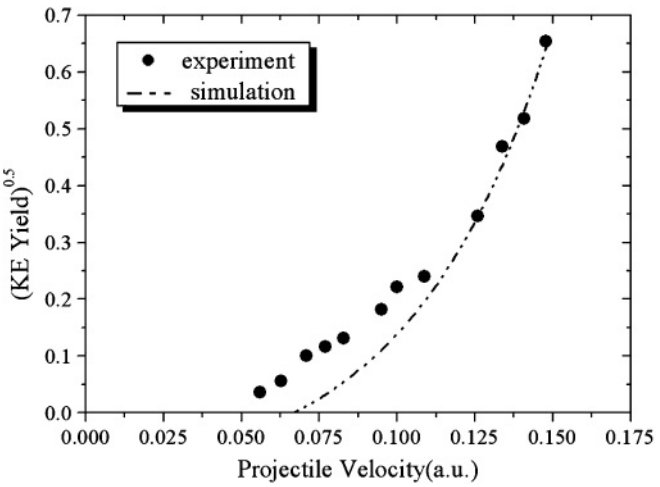

FIG. 6. Square root of KE yields as a function of projectile velocity for atomic projectile Ar° grazing on the Al(111) surface under $\theta_{\rm in} = 2.2°$.

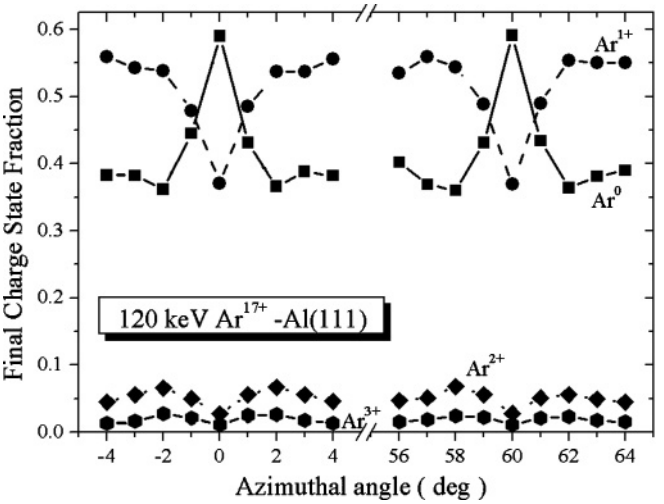

FIG. 7. Final charge-state fractions as a function of azimuthal angles of the crystal surface for 120-keV Ar^{17+} ions grazing on the Al(111) surface at $\theta_{\rm in} = 0.8°$. Azimuthal angles are around $\varphi = 0°$ and $\varphi = 60°$. The lines are drawn to guide the eyes.

through the SF mechanism can be neglected for the filling of K-shell vacancies, but the SF mechanism makes a significant contribution to the filling of L,M-shell vacancies. However, during the interaction of heavy ions with light target solids ($Z_{\rm ion} > Z_{\rm solid}$), the binding energy of the inner-shell solid electrons is smaller than the binding energy of the inner-shell vacancies of ion [18]. Under such conditions, the possibility that the inner-shell vacancies are filled by the side-feeding (SF) mechanism is a matter of discussion, particularly the vacancies with large binding energies. In the following, we will discuss the average contribution through Auger transitions, x-ray decay, and the SF mechanism to the inner-shell filling under the $Z_{\rm ion} > Z_{\rm solid}$ condition.

The final charge-state distributions as a function of azimuthal angles are shown in Fig. 7, and the data clearly show that final charge-state distributions change strongly with azimuthal angles. The fractions of Ar°, Ar^{1+} are prevailing (0.36–0.60) and the fractions of Ar^{2+}, Ar^{3+} are lower than 0.07 for all azimuthal angles. For the two final charged states, Ar^0 and Ar^{1+}, the maximum variations of fractions are 0.23 and 0.185, respectively. For the final charged states Ar°, the dependence on azimuthal angles is enhanced for Ar^{17+} ions grazing along low-index directions. Its fraction is equal to 0.59 at the $\varphi = 0°$ direction, and its values fluctuate at random directions, from 0.37 $\sim$ 0.45. For example, the final charge-state fractions are 0.362 and 0.366 for random directions $\varphi = -2°$, 2°, respectively. The enhancement of the fully neutralization degree of HCI for low-index directions is about 22.4%, compared to random directions.

Figure 8 shows potential electron yields of simulation results with incident kinetic energy 120 keV. For AI, PO, and PL, because 50% electrons are emitted toward the vacuum and the other 50% toward the surface, the total detectable potential electron yields should be halved: $\Sigma = 0.5*(\mathrm{AI} + \mathrm{PO} + \mathrm{PL})$, where AI stands for autoionization electrons emitted above surface, and PO and PL denote the electron emission yields from peeling off and promotion loss, respectively. The potential electron yields are about 26.3 $\sim$ 29.4 per ion. AI

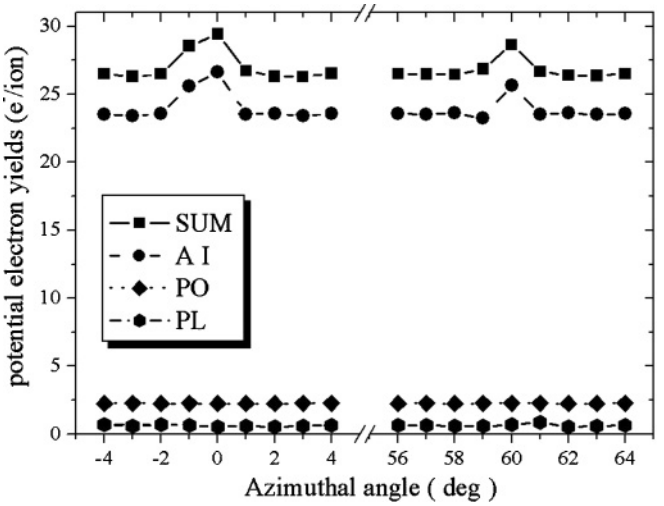

FIG. 8. Potential electron yields as a function of azimuthal angles for 120-keV Ar^{17+} grazing on the Al(111) single-crystal surface. The incident angle is $\theta_{in} = 0.8^\circ$ in all cases. The lines are drawn to guide the eye.

occupies the major part of PEE yields, and the corresponding contributions are about 23.5 ~ 26.6 per ion. For directions $\varphi = 0^\circ$, -2°, 2°, AI yields change from 26.63 to 23.57 and 23.55 per ion. The enhancement of AI yields is 13.0% for low-index direction, compared to random directions. Because when Ar^{17+} ions graze along low-index directions, "axial channeling" happens and there is more time for AI above the surface; as a result, more electrons de-excite to a lower energy level. In addition, the PO and PL yields which contribute minor parts to the PEE yields are almost identical for all incident azimuthal angles

C. X-ray emission

The *K*-shell vacancy decay of highly charged ions Ar^{17+} interacting with metallic surface at grazing incidence also can be studied by investigating *K* x-ray spectra.

According to the simulation results shown in Fig. 9, the main features of the *Kα* x-ray spectra can be summarized as follows:

(i) The intensity of KL^1 lines is the strongest one among these eight satellite lines, and the satellite line distributions mainly concentrate on the KL^1, KL^2 lines. Furthermore, the intensity of KL^x ($x = 3$–8) lines strongly decrease, compared to the KL^1 line. This feature of these spectra is greatly different from the results of d'Etat *et al*. [25] in which many *L*-shell spectator electrons are presented at the time of x-ray emission.

(ii) The dependence of the intensity of KL^x ($x = 1$–2) lines on azimuthal angles is slightly enhanced when Ar^{17+} ions graze along low-index direction $\varphi = 0^\circ$.

The relative intensity of the KL^x lines depends only on the rate at which the *L* shell is filled compared to that for the filling of the *K* vacancies. The *L* filling rate depends on the initial state on which the electrons have been captured and on the initial number of captured electrons. Three electron-capture processes—auger transitions, the side-feeding mechanism, and radiative decay—may make contributions to the filling of *L*-shell vacancies. According to Ref. [18], the L*α* x-ray rate is very small and therefore contributes a very minor part to

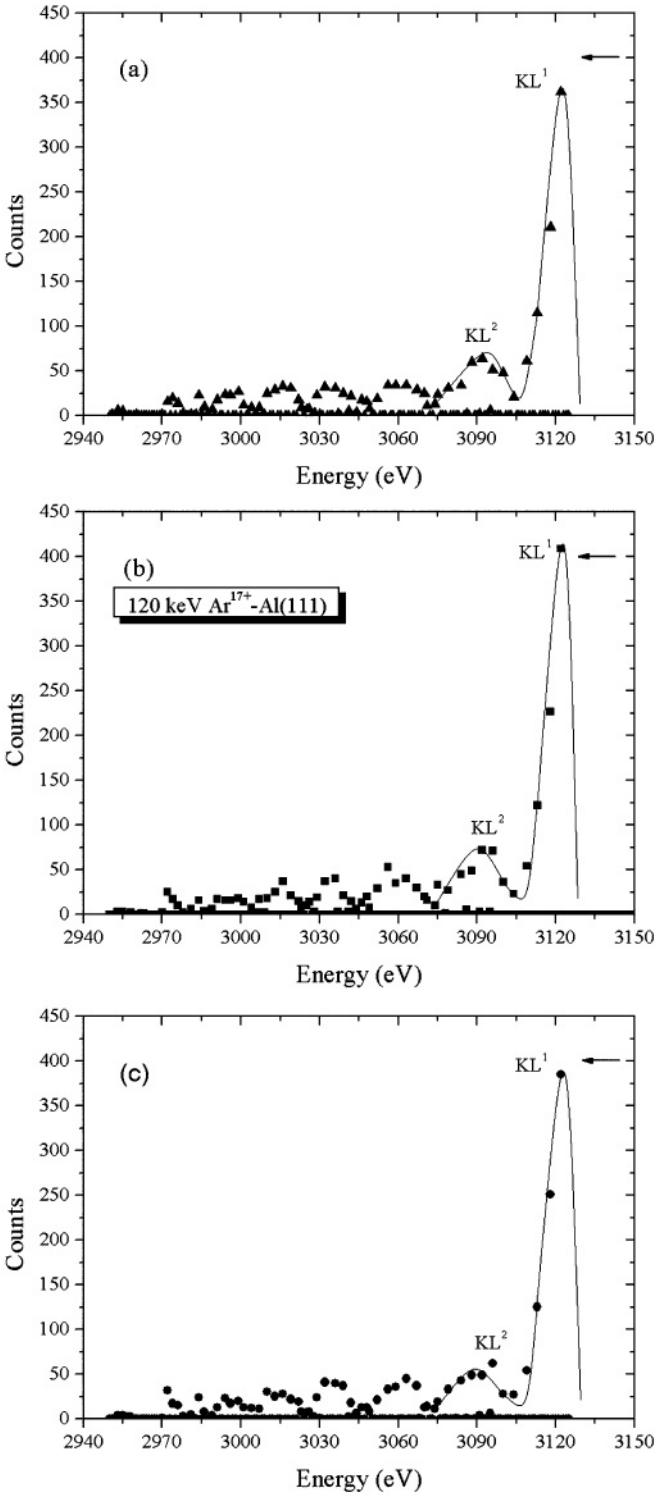

FIG. 9. The K*α* x-ray spectra obtained from 120-keV Ar^{17+} grazing on the Al(111) surface at incidence of $\theta_{in} = 0.8^\circ$. Panels (a), (b), and (c) denote the K*α* x-ray spectra for Ar^{17+} ions grazing under azimuthal angles $\varphi = -2^\circ$, 0°, and 2°, respectively. The solid lines are drawn to guide the eye. The arrow stands for the position of counts number "400."

the *L* vacancy filling. In addition, the Auger transition and *Kα* radiative decay rate are generally too small to allow the filling of the inner shell of the HCI before it reaches the surface.

Therefore, the side-feeding process which is now known as the direct transfer of electrons from target into the inner shells of the HCI plays an important role in the inner-shell electron capture [41]. The side feeding is the inner-shell electron transition between target and projectile, which can only take place in close collisions with the level crossing of inner shells between the HCI and target atoms. For inner shells, the detailed side-feeding rate given in Ref. [41] was adopted.

There are two interpretations for the differences between the present simulated spectra and the spectrum already published in Ref. [25].

(i) When HCI collides with the target surface, considering the matching of the energy level, only the shells of which energy level is lower than the metal Fermi level can get electrons through the side-feeding mechanism. In the work of Winecki *et al*. [18], they excluded the possibility of side feeding into the Ar, *K*, or *L* shells because of the gross mismatch in energy between these levels and carbon binding energies. For the same reason, regarding the simplicity of the present model, only the *M* shells for the side-feeding mechanism is important during the interaction of heavy ions with the light target solids ($Z_{\text{ion}} > Z_{\text{target}}$). Under such conditions, only Auger or x-ray decay would be expected to be responsible for the *K*-, *L*-shell vacancies. Consequently, the *L*-shell vacancies will be filled slowly due to the small de-excitation rates of the long series of Auger transitions, involving many intermediate states. However, the experimental work of d'Etat *et al*. had been performed with heavy metallic targets and light ions ($Z_{\text{Ar}} < Z_{\text{Ag}}$) for which the direct side feeding into *L*-shell vacancies seems quite possible [18]. This indicates that the *L*-shell vacancies may be fed quickly through the side-feeding process. As a result, there are more *L*-shell spectator electrons at the time of x-ray emission.

(ii) At grazing incidence, when SHCI reaches the metallic surface, it may penetrate into or reflect specularly from the surface. In the former case, the corresponding $K\alpha$ spectrum is then the sum of two spectra: one coming from ions which have captured any electrons in high states and have enough time to decay by Auger transitions until a first electron reaches the *L* shell, prior to reaching the surface; and the other one emitted by the ions when they penetrate into the bulk. Because side feeding is a collision the electron-capture process, its rate will be higher at much closer distances when the ions penetrate into the bulk. The *M* and *N* shells are quasi-instantaneously filled up when the HCI enters the surface, and then some of these *M*-shell electrons are very quickly transferred into the *L* shell through LMM Auger transitions (there is just one step and the LMM Auger rates are very large) [46]. Therefore, the $K\alpha$ decay takes place at any time of the *L*-shell filling, and one may observe the $KL^x (x = 1\text{–}8)$ satellite lines in the presence of any number *x* of *L* electrons. However, outside the surface the excited ions mainly decay to the ground state through a long series of Auger transitions involving many intermediates states. The characteristic of this cascade will end up with the arrival of a first electron on the *L* shell. Under such condition, the transition probabilities for a new filling of the *L* shell and the filling of the *K* shell through the emission of, for example, a $K\alpha$ line are comparable [46]. Then one must observe the characteristic x-ray spectra having one (or two) *L* electron.

In the work of d'Etat *et al*. [25], the Ar^{17+} ions with energy 289-keV graze on the silver target under incidence of 6.5°, 4.5°, and 3°. The energies for the motion normal to the surface plane can be obtained by the equation $E_\perp = E_0{}^*\sin^2(\theta_{\text{in}})$ [6] and the corresponding normal energies are 3.7, 1.779, and 0.792 keV for incidence angles of 6.5°, 4.5°, and 3°, respectively. Because the excited ions will spend less time above the surface at higher normal energies, the fraction of outside solid decay decrease with the increasing of $E_\perp$. Therefore, the main part of their spectrum represents what happens inside the solid, and only a small part is due to the interactions outside the surface.

In the present work, the normal energy is 23.4 eV for the interaction of 120-keV Ar^{17+} ions grazing on the Al(111) surface under incidence of $\theta_{\text{in}} = 0.8°$. At such low normal energy, the Ar^{17+} ions will reflect specularly from the topmost surface layer and the excited ion spends all its time above the surface. Therefore, the corresponding $K\alpha$ x-ray spectra represent purely what happens outside the solid, and one would only observe the continuous decrease of the KL^x intensities with increasing value of *x*. In addition, the $K\alpha$ spectrum shown in Fig. 9 is similar to the results of Briand *et al*. [46]. In their work, the x-ray spectrum of 34-eV Ar^{17+} ions impinging on the Au target was investigated and the x ray is mainly generated when the HCI is above or in the first several-atom layer at such low-incident energy [41]. We have to point out that there is still a difference between the present spectrum and the results of Briand *et al*. in which the intensity of the KL^2 line is even larger than that of the KL^1 line. Because the Au target was used in their work ($Z_{\text{Ar}} < Z_{\text{Au}}$), the direct capture of a few electrons to *L* shells becomes quite possible. In addition, the HCI would eventually hit the surface so that the HCI can get close to the target atoms, leading to the direct capture of a few electrons into the *M* shell. Some of these *M*-shell electrons are quickly transferred into the *L* shell through LMM Auger transitions. Therefore, the x rays are generated at a higher number of *L*-shell spectator electrons, which increases the intensity of the KL^2 line.

The dependence of the intensity of the KL^x $(x = 1)$ lines on azimuthal angles is enhanced due to the effect that the effective trajectory length can be prolonged by the axial channeling, and therefore the ion-surface interaction time is longer for grazing along low-index directions as compared to random directions. The x-ray yields are 0.1876, 0.1955, and 0.188 for $\varphi = -2°$, 0°, and 2°, respectively. The enhancement of x-ray yields is about 4.2% for the low-index direction, compared to random directions.

As shown in Table I, the enhancement of AI yields and x-ray yields is 13.0% and 4.2%, respectively, for the low-index direction, compared to random directions. For final charge-state Ar°, the enhancement is 22.4%, which means that more inner-shell vacancies of Ar^{17+} ions are fully filled for $\varphi = 0°$ than for random directions by 22.4%. Three electron-capture processes—Auger transitions, the side-feeding mechanism, and radiative decay—may make contributions to the filling of *K*-, *L*-, and *M*-shell vacancies. Then, the average contribution to inner-shell vacancies through the side-feeding mechanism can be obtained by 22.4% − 13.0% − 4.2% = 5.2%. These results show that the Auger transition is the main contribution to the inner-shell filling, which is in agreement with the results

TABLE I. Enhancement of AI yields, x-ray yields, and final charge-state fractions for highly charged ions Ar^{17+} grazing along low-index direction in comparison with random directions.

	$\varphi = -2^\circ$	$\varphi = 0^\circ$	$\varphi = 2^\circ$	Enhancement
AI	23.57	26.63	23.55	13.0%
X ray	0.1876	0.1955	0.188	~4.2%
Ar°	0.362	0.59	0.366	22.4%
Ar^{1+}	0.537	0.371	0.535	−16.6%

of Fig. 7 in which the fraction of the final-charge state Ar° is lower than 0.6 due to the small de-excitation rate of the Auger transitions. However, from Table I in Ref. [41], the side-feeding mechanism makes the main part to the inner-shell filling contribution, which is different from our results. In their work, the metal Ag whose atomic number is larger than that of incident Ar^{q+} ions was used as the target, and the projectiles will eventually penetrate into the bulk so that the HCI can be very close to the target atom. Under such conditions, the side-feeding rate will be higher and therefore make the main part to the inner-shell filling contribution.

IV. CONCLUSION

The present work simulates the interaction of highly charged ions grazing on the single-crystal Al(111) surface. The screened Coulomb potential and the classical over-barrier model are used to simulate the ion's motion and charge-exchange processes. We have found that the dependence of energy loss, potential electron yields, and intensity of KL^1 satellite lines on azimuthal angles is enhanced for highly charged ions Ar^{17+} grazing along low-index directions. This finding indicates that the surface structure has great influence on SHCI-surface interaction. In addition, the simulated $K\alpha$ x-ray spectra show that the distribution of KL^x ($x = 1$–8) satellite lines peaks toward the lines with small x values, which means that the ion approaching the surface at a small angle is slowly neutralized; consequently, the average L-shell population at the time of x-ray emission is low. The calculated energy loss spectra and KEE yields agree reasonably with the experimental results.

ACKNOWLEDGMENTS

This work is supported by the Program for New Century Excellent Talents in University and the National Natural Science Foundation of China under Grant Nos. 10775062 and 10875054.

[1] C. Lemell, J. Stöckl, J. Burgdörfer, G. Betz, H. P. Winter, and F. Aumayr, Phys. Rev. Lett. **81**, 1965 (1998).
[2] J. I. Juaristi, A. Arnau, P. M. Echenique, C. Auth, and H. Winter, Nucl. Instrum. Methods B **157**, 87 (1999).
[3] A. Mertens and H. Winter, Phys. Rev. Lett. **85**, 2825 (2000).
[4] H. Winter, A. Mertens, R. Pfandzelter, and V. Staemmler, Phys. Rev. A **66**, 022902 (2002).
[5] J. Stöckl, T. Suta, F. Ditroi, H. P. Winter, and F. Aumayr, Phys. Rev. Lett. **93**, 263201 (2004).
[6] H. Winter, Phys. Rep. **367**, 387 (2002).
[7] J.-P. Briand, S. Thuriez, G. Giardino, G. Borsoni, V. Le Roux, M. Froment, M. Eddrief, C. de Villeneuve, B. D'Etat-Ban, and C. Sébenne, Phys. Rev. A **55**, R2523 (1997).
[8] Q. Yan, D. M. Zehner, F. W. Meyer, and S. Schippers, Phys. Rev. A **54**, 641 (1996).
[9] S. Winecki, M. P. Stöckli, and C. L. Cocke, Phys. Rev. A **56**, 538 (1997).
[10] W. Huang, H. Lebius, R. Schuch, M. Grether, and N. Stolterfoht, Phys. Rev. A **58**, 2962 (1998).
[11] H. Winter and F. Aumayr, Mol. Opt. Phys. **32**, R39 (1999).
[12] J. P. Briand, L. de Billy, P. Charles, S. Essabaa, P. Briand, R. Geller, J.-P. Desclaux, S. Bliman, and C. Ristori, Phys. Rev. Lett. **65**, 159 (1990).
[13] N. Stolterfoht, J. H. Bremer, R. Diez Muino, Interaction Journal of Mass Spectrometry **192**, 425 (1999).
[14] J.-P. Briand, G. Giardino, G. Borsoni, M. Froment, M. Eddrief, C. Sebenne, S. Bardin, D. Schneider, J. Jin, H. Khemliche, Z. Xie, and M. Prior, Phys. Rev. A **54**, 4136 (1996).
[15] J. Burgdörfer, P. Lerner, and F. W. Meyer, Phys. Rev. A **44**, 5674 (1991).
[16] L. Wirtz, C. O. Reinhold, C. Lemell, and J. Burgdörfer, Phys. Rev. A **67**, 012903 (2003).
[17] F. W. Meyer, L. Folkerts, and S. Schippers, Nucl. Instrum. Methods Phys. Res. B **100**, 366 (1995).
[18] S. Winecki, C. L. Cocke, D. Fry, and M. P. Stöckli, Phys. Rev. A **53**, 4228 (1996).
[19] H. J. Andrä, A. Simionovici, T. Lamy, A. Brenac, G. Lamboley, J. J. Bonnet, A. Fleury, M. Bonnefoy, M. Chassevent, S. Andriamonje, and A. Pesnelle, Z. Phys. D **21**, 135 (1991).
[20] G. Lakits, F. Aumayr, M. Heim, and H. Winter, Phys. Rev. A **42**, 5780 (1990).
[21] H. Eder, A. Mertens, K. Maass, H. Winter, H. P. Winter, and F. Aumayr, Phys. Rev. A **62**, 052901 (2000).
[22] H. P. Winter, S. Lederer, H. Winter, C. Lemell, and J. Burgdörfer, Phys. Rev. B **72**, 161402(R) (2005).
[23] H. Winter, K. Maass, S. Lederer, H. P. Winter, and F. Aumayr, Phys. Rev. B **69**, 054110 (2004).
[24] I. G. Hughes, J. Burgdorfer, L. Folkerts, C. C. Havener, S. H. Overbury, M. T. Robinson, D. M. Zehner, P. A. Zeijlmans van Emmichoven, and F. W. Meyer, Phys. Rev. Lett. **71**, 291 (1993).
[25] B. d'Etat, J. P. Briand, G. Ban, L. de Billy, J. P. Desclaux, and P. Briand, Phys. Rev. A **48**, 1098 (1993).
[26] S. Winecki, M. P. Stöckli, and C. L. Cocke, Phys. Rev. A **55**, 4310 (1997).
[27] Y.-H. Song, Y.-N. Wang, and Z. L. Miskovic, Phys. Rev. A **63**, 052902 (2001).
[28] L. B. Bridwell, H. J. Hay, L. F. Pender, C. J. Sofield, and P. B. Tracy, Aust. J. Phys. **41**, 681 (1988).
[29] J. Burgdorfer and F. Meyer, Phys. Rev. A **47**, R20 (1993).

[30] K. Tökési, X. M. Tong, C. Lemell, and J. Burgdörfer, Phys. Rev. A **72**, 022901 (2005).
[31] W. Brandt and M. Kitagawa, Phys. Rev. B **25**, 5631 (1982).
[32] C. J. Setterlind and A. Barnay, Nucl. Instrum. Methods Phys. Res. B **98**, 407 (1995).
[33] Y. N. Wang and W.-K. Liu, Phys. Rev. A **54**, 636 (1996).
[34] H. Winter and H. P. Winter, Europhys. Lett. **62**, 739 (2003).
[35] R. A. Baragiola, E. V. Alonso, and A. Oliva Florio, Phys. Rev. B **19**, 121 (1979).
[36] J. Ducree, H. J. Andra, and U. Thumm, Phys. Rev. A **60**, 3029 (1999).
[37] J. C. Slater, Phys. Rev. **36**, 57 (1930).
[38] N. V. Smith, C. T. Chen, and M. Weinert, Phys. Rev. B **40**, 7565 (1989).
[39] A. Dubus, J.-C. Dehaes, J. P. Ganachaud, A. Hafni, and M. Cailler, Phys. Rev. B **47**, 11056 (1993).
[40] A. Miotello and M. Dapor, Phys. Rev. B **56**, 2241 (1997).
[41] J. Wang, J. Zhang, J. Gu, X. Luo, and B. Hu, Phys. Rev. A **80**, 062902 (2009).
[42] C. P. Bhalla, Phys. Rev. A **8**, 2877 (1973).
[43] S. Lederer, H. Winter, and HP. Winter, Nucl. Instrum. Methods B **258**, 87 (2007).
[44] A. Robin, W. Heiland, J. Jensen, J. I. Juaristi, and A. Arnau, Phys. Rev. A **64**, 052901 (2001).
[45] H. P. Winter, F. Aumayr, C. Lemell, J. Burgdorfer, S. Lederer, and H. Winter, Nucl. Instrum. Methods B **256**, 455 (2007).
[46] J.-P. Briand, S. Thuriez, G. Giardino *et al.*, Phys. Rev. Lett. **77**, 1452 (1996).